

This document is the Accepted Manuscript version of a Published Work that appeared in final form in ACS Applied Materials and Interfaces, copyright © American Chemical Society after peer review and technical editing by the publisher. To access the final edited and published work see:
<https://dx.doi.org/10.1021/acsami.6b02896>.

Self-arranged misfit dislocation network formation upon strain release in $\text{La}_{0.7}\text{Sr}_{0.3}\text{MnO}_3/\text{LaAlO}_3(100)$ epitaxial films under compressive strain

José Santiso,^{a,} Jaume Roqueta,^a Núria Bagués,^{a,b} Carlos Frontera,^b Zorica Konstantinovic,^b
Qiyang Lu,^c Bilge Yildiz,^c Benjamín Martínez,^b Alberto Pomar,^b Lluís Balcells,^b and Felip
Sandiumenge.^b*

^aCatalan Institute of Nanoscience and Nanotechnology (ICN2), CSIC and the Barcelona Institute of Science and Technology (BIST). Campus UAB 08193 Bellaterra, Barcelona, Spain.

^bMaterials Science Institute of Barcelona (ICMAB), CSIC, Campus UAB, 08193 Bellaterra.

^cMassachusetts Institute of Technology (MIT), Cambridge, MA

KEYWORDS:

strain relaxation, misfit dislocation arrangement, nanophase modulation, nanotemplate.

ABSTRACT

Lattice-mismatched epitaxial films of $\text{La}_{0.7}\text{Sr}_{0.3}\text{MnO}_3$ (LSMO) on LaAlO_3 (001) substrates develop a crossed pattern of misfit dislocations above a critical thickness of 2.5 nm. Upon film thickness increases the dislocation density progressively increases and the dislocation spacing distribution becomes narrower. At a film thickness of 7.0 nm the misfit dislocation density is close to the saturation for full relaxation. The misfit dislocation arrangement produces a 2D lateral periodic structure modulation ($\Lambda \sim 16$ nm) alternating two differentiated phases: one phase fully-coherent with the substrate and a fully-relaxed phase. This modulation is confined to the interface region between film and substrate. This phase separation is clearly identified by X-ray diffraction and further proven in the macroscopic resistivity measurements as a combination of two transition temperatures (with low and high T_c). Films thicker than 7.0 nm show progressive relaxation and its macroscopic resistivity becomes similar than that of the bulk material. Therefore, this study identifies the growth conditions and thickness ranges that facilitate the formation of laterally modulated nanocomposites with functional properties notably different from those of fully coherent or fully relaxed material.

1. INTRODUCTION

Strain engineering in thin epitaxial films of transition metal oxides with perovskite structure has become an important field of study in the last decade because of the strong correlations between the subtle structure variations induced by the epitaxial growth on mismatched substrates and the electronic properties of oxide films, which have proven to render the film material very different functional properties to those of the equilibrium material.¹⁻⁴

Lattice-mismatched heterostructures of perovskite oxides are also of interest because the regions surrounding the defects generated during the strain relief, typically misfit dislocations or walls between crystal domains with different orientation, very often show a different structure and symmetry than the rest of the film material at the nanoscale.⁵⁻⁷ This may offer a basis for fabrication of a variety of low-dimensional and mesoscopic systems in solid-state physics.⁸⁻¹¹

In epitaxial growth on substrates with lattice mismatch, the film structure is submitted to an in-plane biaxial strain, either compressive or tensile depending on the mismatch with the substrate. The out-of-plane cell parameter is therefore expanded or compressed, as results of an elastic response of the material. According to the classical model by Frank and van der Merwe¹² and Matthews-Blakeslee¹³ the films grow pseudomorphically with the substrate below a certain critical thickness. Above this thickness the film usually releases the accumulated strain energy via plastic deformation, thus generating misfit dislocations (MDs), which progressively accommodate the strain towards the equilibrium bulk structure.¹⁴

At a local scale the strain accommodation by a pure edge dislocation is uniaxial, and was early described by the Peierls-Nabarro model.¹⁵ It follows the in-plane projection of the corresponding Burgers vector perpendicular to the dislocation line. Therefore, the biaxial strain in the films is

necessarily accommodated by the formation of an array of misfit dislocations, as early observed by the concomitant formation of a cross-hatched surface morphology pattern in lattice-mismatched heterostructures of III-V semiconductors like GaAsP/GaAs,¹⁶ which was further theoretically described by Speck and Pompe.¹⁴ This is typically observed in thick films by means of optical or atomic force microscopy, but difficult to trace in very thin films. The observation of misfit dislocations arrays has been more recently reported also in some perovskite oxide heterostructures such as in SrRuO₃/SrTiO₃(100),¹⁷ in buried (Ca_{1-x}Sr_x)(Zr_{1-x}Ru_x)O₃/SrRuO₃/SrTiO₃(100),¹⁸ in La_{0.5}Ca_{0.5}MnO₃/SrTiO₃(100),¹⁹ or in BaTiO₃/SrTiO₃(100).²⁰

In heterostructures that undergo strain relief by the formation of a high density of dislocations, they often arrange into highly ordered periodic patterns. This self-arrangement is induced by the repulsive forces generated in the interaction between misfit dislocations as well as their mobility along the interfaces, which depends on the elastic properties of the material and the deposition conditions. In an ideal case of a perfect periodical arrangement it may provide a route to obtain the size uniformity needed for electronic applications such as in quantum dot arrays.²¹ The dislocation pattern may also serve as a nanotemplate for the guided growth of 2D nanostructured materials, such as demonstrated in the preferential nucleation of Fe and Cu metal particles on strain-relieved Pt(111) [22], the growth of ZnSe nanowires and nanorod structures on GaAs,²³ as well as the growth of exotic nanomaterials seeded by screw dislocations.²⁴

Understanding the formation and self-organization mechanism of such MD arrays in oxide perovskite materials is important for the fabrication of low-dimensional structures, thus providing an opportunity for the finding of novel physical phenomena. One perfect example is the recently reported condensation of two-dimensional oxide-interfacial charges into one-

dimensional electron chains induced by the misfit-dislocation strain field in $(\text{Nd}_{0.35}\text{Sr}_{0.65})\text{MnO}_3/\text{SrTiO}_3$.¹¹

This paper aims to investigate the progressive self-organisation of the misfit dislocation network occurring during the epitaxial growth of a heterostructure of complex oxide materials with perovskite structure submitted to a large biaxial compressive stress, exemplified by $\text{La}_{0.7}\text{Sr}_{0.3}\text{MnO}_3$ (LSMO) grown on LaAlO_3 (100) substrates (LAO). The strain modulation observed in ultrathin nanostructured films of LSMO material is correlated with the measured magnetotransport behaviour.

2. EXPERIMENTAL METHODS

$\text{La}_{0.7}\text{Sr}_{0.3}\text{MnO}_3$ films with different thickness from 2.0 to 14.0 nm were deposited by RF magnetron sputtering under the same conditions and experimental setup as described in previous works.^{25, 26} LaAlO_3 (100) crystals (Crystec, GmbH) were used as substrates. The surface morphology along with the formation of misfit dislocations was examined by atomic force microscopy (PicoSPM, Molecular Imaging, in tapping mode) and scanning electron microscopy (Quanta 200 FEG-ESEM, FEI). Detailed observations of the strain fields induced by the presence of the misfit dislocations were obtained by transmission electron microscopy in HAADF (high angle annular dark field) mode, as well as high-resolution TEM planar images (field emission gun Tecnai F20 S/TEM, FEI at 200kV). High resolution TEM images of film cross-section were obtained in a Cs-corrected microscope (F20 Tecnai, FEI). The overall film structure and the features induced by the arrangement of the misfit dislocation network was analysed by X-ray diffraction making use of laboratory diffractometers (Panalytical X'Pert

MRD, Rigaku SmartLab) for standard and in-plane diffraction geometry. 2D X-ray reciprocal space mapping experiments were performed on beamline BM25 at the European Synchrotron Radiation Facility (ESRF), Grenoble, France. 3D XRD reciprocal space maps were carried out by using synchrotron radiation at the KMC-2 beamline at Helmholtz-Zentrum Berlin (Bessy II). Resistivity of the films was measured as a function of temperature, from 10 to 380 K in absence of magnetic field ($H=0\text{T}$) and in presence of a magnetic field of $H=9\text{T}$ by using a physical properties measurement system (PPMS) from Quantum Design.

3. RESULTS AND DISCUSSION

All deposited films are continuous and show essentially flat morphology with single unit cell step terraces, as revealed by topography images obtained by AFM as depicted in Figure 1(a) for the LSMO/LAO film of 7 nm thickness. A closer observation of the morphology of this film reveals the presence of a dense cross-hatched pattern following two perpendicular directions (corresponding to $[100]/[010]$ main crystallographic directions), which form subtle ridges of less than one unit cell height. Figure 1(b) shows the orientation contrast SEM image of the same 7nm thick film. As in previous AFM image, it shows a clear contrast forming a crossed pattern of parallel lines following $[100]/[010]$ crystallographic directions. Due to the low film roughness and the absence of secondary phases, the corresponding SEM image shows only contrast related to crystallographic defects or strain fields. These lines presumably correspond to the presence of buried misfit dislocations (MDs) at the interface between film and substrate generated because of the partial release of the misfit strain. A planar view STEM image of that film in high angle annular dark field mode (HAADF) is presented in Figure 1(c). Again it shows a clear contrast

forming lines running parallel to [100] and [010] main directions of the cubic primitive perovskite cell, in agreement with AFM and SEM observations. The bright lines in the HAADF image coincide with the position of the MDs core lines. The distance between dislocations is quite regular in the depicted area and spans from 20 to 30 nm.

High resolution TEM observations of planar view and cross-section of the 7 nm LSMO/LAO film are shown in Figure 2 (a) and (b), respectively. The planar view shows a high crystal quality with atomic column resolution. The dark and white contrast is related to the strain field caused by the misfit dislocations and shows a complex pattern already observed in the lower magnification image in Figure 1(c). The cross-section image evidences the presence of one misfit dislocation core at the interface between film and substrate. The Burgers circuit around the MD core indicates a Burgers vector $\mathbf{b} = a_{\text{LAO}}[100]$ parallel to the interface with magnitude equal to one primitive unit cell of the LAO substrate, which is typical in perovskite oxides and was previously reported in LSMO/LAO.²⁷

3.1. Evolution of misfit dislocation distribution with film thickness

For a comparison of the MDs density evolution Figure 3(a) shows orientation-contrast SEM images of the LSMO films deposited on LAO substrates with different thicknesses from 2 nm to 14 nm. OC-SEM images offer a direct method to reveal the presence of MDs pattern clearer than AFM and much simpler to prepare than TEM planar view specimens.

The thinnest film of 2 nm does not show any evidence of misfit dislocation formation. However, the film with 3.5 nm thickness already shows a pattern of lines corresponding to MDs with different spacing. Films with larger thickness of 7 and 14 nm show a dense distribution of crossed MDs forming a regular grid. Therefore, from these images it can be estimated that the

critical thickness for the formation of MDs lies roughly between 2.0 and 3.5 nm, and the films progressively show a higher MD density with thickness.

In order to quantify the MDs distribution Figure 4(a) shows histograms of their spacing obtained from a large number (about 190) of linear scans across the SEM images. They consist of a single mode Poisson distribution with different mean and standard deviation values, as opposed to the bimodal distributions often observed in semiconductors (in the diluted MD dislocation regime) and related to the interaction between 60° dislocations with opposite in-plane component to form pure edge dislocations.²⁸ The film with 3.5 nm thickness shows a mean dislocation separation around 38 nm, corresponding to a dislocation linear density of $2.6 \cdot 10^5 \text{ cm}^{-1}$, while for the 7 nm and 14 nm thick samples the mean separations were 25 nm and 16 nm, respectively (linear dislocation densities around $4.0 \cdot 10^5 \text{ cm}^{-1}$ and $6.2 \cdot 10^5 \text{ cm}^{-1}$). For thicker films the image of the dislocation gets blurred because of the limited penetration depth of the electrons and it is difficult to accurately measure their separation by SEM. In a fully relaxed LSMO film (with cell parameter $a_{\text{LSMO}} = 3.885 \text{ \AA}$, and pseudocubic cell parameter $a_{\text{LAO}} = 3.790 \text{ \AA}$ for the LAO substrate), a simple calculation gives a saturation misfit dislocation density of $6.45 \cdot 10^5 \text{ cm}^{-1}$, assuming a Burgers vector equal to one unit cell in the direction parallel to $[100]$, $\mathbf{b} = a_{\text{LAO}}[100]$. This corresponds to one misfit dislocation every 40 u.c. of the LSMO structure, i.e., an average MD separation of 15.5 nm. The mean values of the experimental linear dislocation density progressively increase with thickness reaching almost full relaxation for the 14 nm thick sample. Figure 4(b) depicts that density as a function of the reciprocal film thickness. The dependence is roughly linear following the expression:

$$\rho_{MD} = \rho_{relaxed}(1 - h_c/h) \quad (1)$$

above a critical thickness h_c before it reaches saturation at the maximum dislocation density for the fully relaxed films, consistent with Matthews and Blakeslee model.¹³ The critical thickness value can be extrapolated from the $\rho_{MD} = 0$ intercept to be roughly 2.5 nm.

From thermodynamic equilibrium considerations Matthews and Blakeslee derived a self-contained expression for the critical thickness, h_c ²⁹

$$h_c = \frac{b}{4\pi f} \frac{(1 - \nu \cos^2 \theta)}{(1 + \nu) \sin \theta \cos \phi} \ln \left(\frac{\alpha h_c}{b} \right) \quad (2)$$

where b is the modulus of the Burgers vector, f is the magnitude of the strain, ν is the Poisson ratio, and θ and ϕ are the angles between the Burgers vector and the dislocation line and the interface plane, respectively. The value of the dislocation core parameter, α , may vary between $\alpha=1$ and $\alpha=4$, and in practical cases, it is obtained from experimental data. As an estimate, in this case, we assume the value of $\alpha=2.72$ first derived in the Matthews and Blakeslee theory.²⁹ The values of $b = 3.885 \text{ \AA}$ (1 u.c.), mismatch $|f| = 0.024$, $\theta = 90^\circ$, $\phi = 0^\circ$, were taken for the present case of LSMO/LAO. The Poisson ratio was calculated from the experimental LSMO cell parameters of the fully-strained 2.0 nm film measured by high resolution XRD $2\theta/\omega$ scans (out-of-plane $c = 3.885 \text{ \AA}$; in-plane $a=3.790 \text{ \AA}$). Assuming an equilibrium cell structure $a= 3.885 \text{ \AA}$, the corresponding strains are $\varepsilon_{//} = -0.0244$; $\varepsilon_{\perp} = +0.0257$, and the Poisson ratio calculated from the expression for biaxial strain $\varepsilon_{\parallel} = -(2\nu/1 - \nu) \varepsilon_{\perp}$ ³⁰ was $\nu = 0.32$. Therefore, a critical thickness of $h_c = 1.7 \text{ nm}$ is obtained from eq.(2), which is slightly below the experimental observation.

The standard deviation of the distribution of MD separation depicted in Figure 4(a) also varies with film thickness, being very wide for the 3.5 nm thick sample, which is about 18 nm. The standard deviation distribution becomes gradually reduced to about 9.5 nm and 3.6 nm for the 7 nm and 14 nm thick samples, respectively. The same graph in Figure 4(b) shows an almost linear dependence of the distribution standard deviations with the reciprocal thickness approaching to a zero value for the thicker films, which indicates the trend towards a perfect arrangement of the misfit dislocation network. At the critical thickness the distribution deviation extrapolates to very large values, which essentially indicate that at the very onset of the misfit dislocation formation their distribution is flat with random separation distance between them. Upon the MD density increases their strain fields interact progressively narrowing their distribution until they self-arrange forming a highly ordered crossed network already at a film thickness of 7 nm.

It is also interesting to notice that in the 3.5 nm thick film, where the misfit dislocation density is low and the self-arrangement is far from being complete, the misfit dislocations show also a wide distribution in length from long segments of several hundreds of nanometres to short dislocations of only a few tenths of nanometres, as evidenced in Figure 3(a). Some MDs end within the film, although most of the MDs end when they meet another orthogonal MD line. This observation is consistent with the finding previously reported in SiGe and III-V semiconductors where the ends of the misfit dislocations turn into threading dislocations half loops emerging at the film surface.³¹ In a regime with low density of misfit dislocations the threading dislocations loops do not get annihilated and they persist in the film, their lateral diffusion being blocked by the strain field of some other crossing misfit dislocation. Upon increasing the MD dislocation density the threading dislocations have larger probability to overcome those barriers, eventually meeting another threading dislocations and annihilate each other, turning into longer sections of

MD lines. In the 7 nm film, short length MDs are rare, and most of them extend for hundreds of nanometres, as observed in the SEM and TEM images in Figure 1(b) and (c).

3.2. Structure lateral modulation

It is difficult to accurately measure the in-plane cell parameter for ultrathin films of only a few nanometres thickness by reciprocal space mapping, because of their very weak signal and the overlap with the intense substrate peaks. Instead, the in-plane diffraction geometry (with grazing incidence and exit angles) allows for a qualitative insight into the in-plane cell parameter relaxation. This provides an alternative way to indirectly measure the MD density. Figure 3(b) and (c) show in-plane 2θ - ϕ area scans of 200 and 110 in-plane reflections, respectively. Any variation in the Bragg peak position along the horizontal 2θ -axis corresponds to a change in the in-plane cell parameter, while a variation in the vertical ϕ -axis most likely corresponds to some tilt in the structure. The 200 area scans of the 2.0 nm thick film shows one single peak at around $2\theta = 48^\circ$ that corresponds to the same position expected for the LAO substrate. The slight elongation of the spot along [110] corresponds to an instrumental origin coming from the X-ray optics. The presence of one single peak indicates that the film in-plane cell parameters are coherent with those of the substrate, and therefore the film is fully strained. Although this grazing angle geometry is intended to enhance the diffracted signal from the topmost part of the film, the penetration of the X-rays still gives a non-negligible overlap with the peak from the substrate for very thin films of a few nanometres. The same occurs for the corresponding 110 area scan where only one peak is observed. However, the 200 and 110 area scans of the 3.5 nm thick film show a considerable diffuse scattering at lower 2θ angles from the substrate peak, which points to an incipient relaxation of its in-plane cell parameter (red arrows). Interestingly,

the diffuse scattering in the 110 area scan shows two different branches following [100] and [010] orthogonal directions (yellow arrows). This is an indication of the uniaxial relaxation character due to the presence of the crossed misfit dislocations.

The 200 and 110 area scans of the 7.0 nm and 14 nm thick films show a very sharp reflection corresponding to the LAO position (at larger 2θ angle, on the right of the scan), and a broader intense reflection (at lower 2θ angle, on the left) corresponding to the partially relaxed LSMO structure (red arrows). This peak position in the maps indicates that in-plane LSMO cell parameters relax equally along [100] and [010] directions, thus keeping a square basal a/b plane. The corresponding cell parameters were measured to be 3.865 and 3.877 Å, for the 7.0 nm and 14 nm thick films, respectively. Taking these values, the number of unit cells between dislocations are calculated as $N=50$ and 44, corresponding to distances 19.5 and 17.0 nm, respectively. These values are in good agreement with those calculated from the SEM observations previously shown in Figure 3(a) and included in Fig 4(b).

Along with the main Bragg peaks these area scans show additional features, as indicated by yellow arrows. In the 200 area scans, between the substrate and film peak positions, there is a clear peak. This peak does not correspond to a Bragg peak. Instead, it corresponds to a first-order satellite peak coming from a lateral structure modulation within the film plane induced by the presence of the dislocation network. Those satellites are also observed in the in-plane XRD maps of the 110 reflection. They deviate from the [110] directions and split in ϕ angle (vertical axis in the scans) following the [100] and [010] directions, as in the thinner 3.5 nm film. This splitting corresponds to the previously mentioned modulation along the plane of the sample, along both [100] and [010] directions. The distance in the reciprocal space between the first

satellite position and the zero order position (on the LAO position) was an indication of the modulation periodicity. For the 3.5, 7 and 14 nm thick LSMO films the modulation period was calculated to be 40 (± 13), 18(± 2) and 17(± 2) nm, respectively, in good agreement with the separation between misfit dislocations. The corresponding MD linear densities for these data were also incorporated in Figure 4(b).

A clearer view of the satellite pattern induced by the modulated structure is observed in the HK reciprocal space maps of the H01 reflections of the 7nm thick film shown in Figure 5(a) for H= 1, 2 and 3. H, K and L axes correspond to the [100], [010] and [001] directions, respectively (H,K and L are expressed in reciprocal lattice units of the LAO substrate). These measurements were performed by using synchrotron radiation and were taken at the L= 0.95 position optimized for the LSMO film, slightly lower than the substrate position at L= 1, because in the relaxed LSMO structure the *c*-axis parameter is larger than that for LAO. The sharp reflections at the (H= 1, K= 0) position along with (H= 2, K= 0) and (H= 3, K= 0) for in the 101, 201 and 301 maps, respectively, correspond to the LAO substrate overlapped with the fully strained LSMO component. The intense reflections at (H= 0.98, K= 0), (H= 1.96, K= 0) and (H= 2.94, K= 0) for the 101, 201 and 301 maps, respectively, correspond to the LSMO partially relaxed Bragg component. The rest of the peaks correspond to satellite reflections in positions (H= $H_0 \pm nd$, K= $0 \pm md$) centred at the H_0 position of the fully coherent LSMO structure, being (n,m) the order of the satellite reflections along H and K directions in the map, respectively. The distance *d* between satellites along H and K shows a constant value of about 0.019 (in reciprocal space units) for all H 0 1 reflections, which is consistent with a square-shape in-plane modulation with periodicity $\Lambda \sim 20$ nm along both [100] and [010]. This is consistent with the presence of the crossed pattern of perfectly parallel misfit dislocations network. First order satellites are clearly

visible, while second or third order satellites are only visible in the proximity of the LSMO partially relaxed reflection.

Figure 5(b) shows the intensity profiles along linear H scans at $K=0$ for the different H01 reflections ($H = 1, 2, 3, 4$ and 5). The scans have been translated so the position of the corresponding H01 LAO reflection coincides for all them at $H-H_0=1.0$. It is clear that satellite reflections (up to second order on the left part of the scan, indicated by the dashed vertical lines) keep the same separation in reciprocal space with respect to the central zero order ($H-H_0=1$) reflection, which is consistent with the in-plane modulation. The curves also show a broad component (indicated with arrows in the graph) progressively shifted to lower H values, from 101 to 501 reflections that corresponds to the Bragg component of the LSMO partially relaxed structure. The inset shows the same scans reduced by dividing by the corresponding H_0 value of the reflection. As expected, all the Bragg components show the same value at around $H/H_0=0.98$ corresponding to an average in-plane cell parameter of 3.864 \AA .

It is not surprising to notice that the partially relaxed LSMO component at the 101 and 201 reflections coincide with the position of $n = -1$ and $n = -2$ ($m = 0$) satellite reflections, respectively. In fact for a fully relaxed LSMO structure we might expect a dislocation distance Λ equal to $\Lambda = N a^{LSMO} = (N + 1)a^{LAO}$; where N is the number of unit cells of LSMO to exactly match $N+1$ cells of LAO. And therefore, in the reciprocal space the position of the n^{th} order satellite will correspond to $Q_x^\Lambda = n \left(\frac{1}{N+1} \right) \left(\frac{1}{a_{LAO}} \right)$. For a couple of HKL reflections of LSMO film and LAO substrate, their corresponding positions along $[100]^*$ direction in the reciprocal space are $Q_x^{LAO} = H \frac{1}{a_{LAO}}$, and $Q_x^{LSMO} = H \frac{1}{a_{LSMO}}$. If we calculate their separation in the reciprocal space $\Delta Q_x^{LAO,LSMO} = (Q_x^{LAO} - Q_x^{LSMO}) = H \left(\frac{1}{N+1} \right) \left(\frac{1}{a_{LAO}} \right) = (H/n) Q_x^\Lambda$. In this way,

for a fully relaxed film, we should expect a perfect coincidence of the modulated structure when $H=n$. Since the 7nm thick film is close to full relaxation we observe such coincidence at $n=1$ for the $H=1$ (101) reflection, and $n=2$ for the $H=2$ (201) reflections.

The overlap of these reflections enhances the intensity of the satellites, along with those at $m = \pm 1$ (along [010]* direction). This is an indication of some degree of constructive interference between the scattered waveforms of both fully strained and fully relaxed LSMO components. As depicted in the sketch in Figure 5(c) the pattern may be described as the overlap between i) a fully strained LSMO contribution coherent with the LAO substrate, with the corresponding square shape satellite pattern generated by the MD periodicity (in blue), ii) plus the partially relaxed LSMO component moving along H, depending on the H01 reflection, (in red colour). Since part of the partially-relaxed structure is also modulated with the same periodicity it is not surprising that it reproduces the same satellite square pattern but centred in the LSMO reflection, with a certain coincidence in some satellite positions. In this way the region around this last component (indicated as the dashed circle) enhances the intensity of the close satellite reflections.

In order to follow in more detail the progression of the misfit dislocation generation and the degree of order of the strain pattern upon film thickness increase, reciprocal space HK maps of the 101 and 111 reflections were collected, by using synchrotron radiation (at constant $L=0.95$, as optimized for the LSMO signal), on the samples with 2.0, 3.5 and 7.0 nm thickness, as shown in Figure 6. Similarly to the in-plane 200 and 110 maps depicted in Figure 3(b) and (c), the 101 and 111 HK maps of the film with 2.0 nm, in Figure 6(a) and (d), show one single peak at ($H= 1$, $K= 0$) and ($H= 1$, $K= 1$), respectively, with no evidence of relaxation. These 101 and 111 reflections were optimized at $L=0.95$ where film signal is maximum, thus minimizing the

overlap with the very narrow LAO rod whose maximum is at $L=1$. The HK maps of the 3.5 nm thick film, shown in Figure 6(b) and (e), present diffuse scattering around the central position following [100] and [010] directions. Since the periodical arrangement of the dislocations is not yet established, the diffuse scattering associated to the linear defects shows broad branches. The substantial asymmetry of the map showing larger intensity tails at $H= 0.98, K= 0$, for the 101 map (left branch in Fig 6 b), and $H= 0.98, K= 1$ and $H= 1, K= 0.98$ values, along the corresponding crossed branches in the 111 map (in bottom and left quadrant of Figure 6 e), points to the uniaxial relaxation of the structure around each set of misfit dislocations. Still, there is a weak contribution to the biaxial relaxation visible in the 111 map along the [110] bisect direction at $H= 0.98, K= 0.98$. The very weak intensity of the branches at larger H and K values is the reason why they were not previously observed in the in-plane maps measured in the lab diffractometer with a conventional $\text{CuK}\alpha$ tube source. The film with 7.0 nm thickness, in Figure 6(c) and (f), shows already a clear biaxially relaxed peak at $H= 0.98, K= 0$, for the 101 map, and $H= 0.98, K= 0.98$ for the 111 map. As in previous observations the periodical arrangement of the crossed misfit dislocations defines clear first order satellites around the central position. Again, the asymmetry between the intensities of the satellites is related to the degree of coherence between relaxed and strained LSMO structures, as explained in the model in Fig 5(c). This makes particularly intense first order satellites at $(H= 0.98, K= 1)$ and $(1, 0.98)$ positions for the 111 map, as well as particularly intense second order satellites in the 101 map at $(H= 0.98, K = \pm 0.02)$ positions.

It is important to point out that the representation of the different HK maps at constant L value has some difficulties given the fact that the optimal value of L for maximizing the intensity of the reflection corresponding to the relaxed part of the LSMO structure is not exactly the same as

for the LSMO structure coherent with the substrate. Since these structures are submitted to a different in-plane biaxial strain they show different out-of-plane c-axis parameter. Similarly, the satellite reflections show a maximum intensity at different L position. Therefore it is more adequate to represent them in 3D. A collection of these 3D representations is shown in the supplementary information.

3.3. Depth distribution

Up to this point we have described the LSMO/LAO films as a combination of a LSMO relaxed structure and a largely strained structure modulated by the presence of the MD network. It is very likely to expect that the modulated structure is in close proximity of the MD lines, and therefore close to the film-substrate interface, while the relaxed LSMO part may be at a certain distance from the dislocations close to the film surface. This difference along the depth of the sample was explored by grazing incidence in-plane diffraction by varying the incidence angle, and therefore the penetration depth of the X-rays. Figure 7(a) shows the linear 2θ - χ scan around the 200 in-plane reflection of the 7nm thick LSMO/LAO film for different ω incidence angle from 0.1 to 0.5°. The scans show the three components: relaxed LSMO at 2θ - χ = 47.0°, fully strained LSMO with a possible overlap with LAO substrate at 2θ - χ = 48.0°, and the intense first order satellite of the modulated structure at 2θ - χ = 47.5°. The overall intensity of the scan increases with the penetration depth. However, the relative intensities of the peaks vary with the incidence angle. Figure 7(b) depicts the relative intensity of the integrated area of the first order satellite peak compared to the relaxed LSMO reflection. The increase of this ratio with the incidence angle indicates that the relaxed LSMO part is closer to the film surface, while the

modulated part is found deeper in the film. The sketch in Figure 7(c) schematically represents the distribution of the two different phases. It is very likely that there is not a clear separation between these phases and there is a gradual change in strain between the top surface and the bottom interface of the film. The real situation may be even more complex if taken into account the strong strain field in the proximity of the MD cores. These may induce sudden changes in the sign of the linear strain but also in the shear strain, probably giving rise to more complex microstructure involving some local monoclinic distortions.

3.4. Influence on film functionality

The macroscopic observation of the planar resistivity in the films also evidences the formation of a distribution of two different phases. Figure 8 shows the resistivity of the films with different thickness from 2 nm to 14 nm at $H=0\text{T}$ (black) and $H=9\text{T}$ (red). The application of a magnetic field strongly enhances ferromagnetic correlations and the associated decrease of resistance gives rise to the so-called Colossal Magnetoresistance (CMR) effect. This response achieves its maximum close to the ferromagnetic (metallic) – to – paramagnetic (insulating) phase transition, i.e., to the corresponding ferromagnetic transition temperature T_c . We observe from Figure 8 that there is a clear evolution of transport properties when film thickness is increased from an insulating-like behaviour for ultrathin films to a ferromagnetic-metallic behaviour typical of LSMO bulk for thicker films. Films with intermediate thickness, namely 3.5 nm and 7 nm films, exhibit more complex magnetotransport properties that, nevertheless, can be easily understood in terms of the distorted structure (average measured c/a cell parameter ratio), as reported in ²⁷ and the presence of the dislocations network in these films. The thinnest film of 2.0 nm exhibits a highly resistive (insulating) behaviour with no sign of ferromagnetic correlations in the range of temperatures available, thus suggesting a non-magnetic character. In the absence of misfit

dislocations this film is in a coherently strained state with a very large c/a ratio ~ 1.06 . In this situation, the extremely distorted octahedral environment is expected to promote selective orbital occupancy and electronic localization thus leading to an antiferromagnetic-insulating behaviour.³² When thickness increases up to 3.5 nm and 7 nm, conductivity is enhanced and magnetoresistive response appears as magnetic field promotes ferromagnetic correlations and electronic delocalization. Thus, it is reasonable to ascribe this behaviour to the appearance of the dislocation network and the coexistence of a poor conducting phase in the distorted region between dislocations and a progressively increasing phase with reduced distortion and improved conductivity. In this way, the alternate arrangement of the dislocations leads to a complex conducting behaviour of two competing phases with different resistances. At 3.5 nm, the relative extent of the insulating phase is large enough to block current paths at zero field (see Figure 8) but this blocking is overcome with the application of magnetic field. At 7 nm, both phases are of similar volume which is manifested by the two distinct maxima in the resistance (around 150 K and 320 K), each of them reflecting their corresponding transition temperature. For the thicker film (14 nm) bulk-like metallic behaviour is recovered and a single transition temperature is observed close to 330 K. In this case, the dominant undistorted phase governs the magnetotransport probably percolating through the whole sample since remnant distorted areas are confined to the interface region between film and substrate, as described in the sketch in Fig 7(c). Therefore, in terms of their transport properties, there is a limited range of film thickness for the macroscopic manifestation of the nanophase mixture of phases.

3.5. Mechanism for misfit dislocation formation

Another striking observation of the LSMO films grown on LAO is that no twin formation was present in the whole range of thickness analysed. This is clearly in contrast with previous

observations of homogeneously twinned LSMO films with total absence of misfit dislocations when deposited on SrTiO₃ (STO) substrates at the same deposition conditions.^{25, 26} This different film microstructure on LAO substrates is explained in terms of the competition between the misfit dislocations and twin domain formation mechanisms.

Misfit dislocations are generated during film growth at elevated temperatures depending on the film-substrate mismatch and film thickness. Little variations are expected to occur beyond that step once an equilibrium misfit dislocation pattern is achieved. At 900 °C, close to the LSMO rhombohedral-to-cubic transformation, shear distortion is less than 0.05° as measured in LSMO/STO films in air.²⁶ Under these conditions no twin domains are expected to form. Subsequently, the twin domains nucleate during the cooling step upon release of the progressively increasing shear stress of the LSMO rhombohedral film structure. The distorted structure nuclei grow until they meet another transformed domain. In LSMO films with no misfit dislocations when grown on STO, the rhombohedral domains compete with each other and arrange forming a homogenous distribution of striped twin domains, thus achieving a long range order depending on the crystal quality of the original crystal matrix. In LSMO/STO striped twin domains were observed from early stages of the growth (above 2.0 nm thickness). However, in the LSMO films on LAO, since a high density of misfit dislocations is already formed at high temperature, the growth front of the transformed nuclei is most likely confined by the strain field originated by the buried misfit dislocations, particularly in ultrathin films. Therefore, it is blocking the long range order of the twin domains and no striped microstructure is achieved. Only sufficiently thick films may transform generating a distribution of twin domains once the influence of the buried misfit dislocations is minimized.

There are several competing mechanisms causing that LSMO films on STO did not show any evidence of misfit dislocation formation, even at film thicknesses as large as several hundreds of nanometres (despite of the critical thickness value $h_c \sim 5$ nm calculated from eq.2 assuming a +0.7% tensile strain of LSMO on STO). This is evidently in contrast with the early formation of misfit dislocations on LAO. In a previous work it was described that in LSMO/STO the tensile strain is accommodated by an enrichment of the Mn^{3+} oxidation state at the interface, thus enlarging the equilibrium cell volume.²⁵ In the absence of a La/Sr composition segregation the charge is compensated by the generation of oxygen vacancies. This reduces the film-substrate mismatch avoiding the formation of misfit dislocations. However, this mechanism is precluded for the -2.4% compressive strain on LAO, because the necessary cell volume reduction, which could be induced by the enhancement of Mn^{4+} oxidation state, cannot be compensated with an oxygen excess. Moreover, it cannot be ruled out that the absence of misfit dislocations in the LSMO films under tensile strain may be also related to an enhancement in the energy barrier for their nucleation and diffusion in comparison to films under compressive biaxial stress. This is not surprising and was already described in early studies. Generally, in semiconducting materials, and to a lower extent in metal heterostructures, there were observed some discrepancies on the critical thickness between the standard models and the experimental density of dislocations, which were attributed to non-negligible energies for the misfit dislocation nucleation at the free surface of the film, as well as for their propagation towards the film-substrate interface.²⁹ The dislocation nucleation energy depends largely in the sign of the stress and the critical thickness for MD nucleation is generally smaller for compression than under tension.³³ The fact that the experimental critical thickness obtained in these series of LSMO/LAO samples, $h_c = 2.5$ nm, does not deviate too much from that calculated from a

thermodynamic equilibrium model of 1.7 nm, is an indication that under compression there are not substantial barriers for misfit dislocation nucleation and propagation, as opposed to the growth LSMO under tension.

4. CONCLUSIONS

In summary, we have observed that LSMO/LAO under large compressive strain of -2.4% starts relaxing forming misfit dislocations from a critical thickness of about 2.5 nm. Progressively, the misfit dislocations density increases, following the expected linear dependence with the reciprocal thickness. At high enough linear densities, above $5 \times 10^5 \text{ cm}^{-1}$, they self-arrange to form a periodic crossed network of edge dislocations with a very narrow distribution of distances. The highly ordered defect structure produces a lateral superperiodicity in the films that can be readily analysed by X-ray diffraction in perfect correlation with the direct observation of the misfit dislocation lines by scanning and transmission electron microscopy. The presence of such high density of misfit dislocations blocks the formation of long striped twin domains. It is very likely that at a local scale the material transforms to the rhombohedral equilibrium structure. However, for the very thin films analysed in this work, the domains are constrained within the nanoscale square regions flanked by crossed misfit dislocations and twin walls were not observed. Within these small regions the concurrence of domains with uniaxial relaxation in perpendicular directions very likely induces a complex pattern of cell distortions as exemplified in the strain contrast pattern of the planar view images in Figures 1(c) and 2(a). The accurate description of this pattern falls beyond the scope of this study and is intended for further work, in correlation with high resolution planar view TEM images. The highly ordered distribution of nanophases with a different cell distortion results in the simultaneous appearance of low and high T_c transition temperatures in the resistivity curves, but only in a limited range of film thickness.

The achievement of a control over the defect arrangement along with the confinement of the rhombohedral-cubic transformation at the nanoscale may produce a combination of metastable phases with unique physical properties, as well as to serve as a template for subsequent heterostructures with lateral periodicity.

FIGURES

Figure 1. Planar view images of a 7 nm thick LSMO/LAO thin film with a well-developed misfit dislocation pattern as observed by AFM topography (a), orientation-contrast SEM (b) and STEM taken at HAADF mode (c). In all cases the image contrast defines parallel lines that correspond to the position of the misfit dislocation cores parallel to [100] and [010] directions.

Figure 2. High-Resolution TEM images of a planar view (a) and cross-section (b) of a 7 nm thick LSMO/LAO film. The cross-section shows a Burgers circuit around a misfit dislocation core at the film-substrate interface with a Burgers vector $\mathbf{b} = a_{\text{LAO}}[100]$.

Figure 3. The chart shows details of LSMO films with different thicknesses from 2, 3.5, 7 and 14 nm. In columns (from left to right): (a) Orientation contrast-SEM images of the same

samples. The observed horizontal and vertical lines correspond to misfit dislocations running parallel to [100] and [010] crystallographic directions; In-plane XRD 2θ - ϕ area of 200 (b) and 110 (c) reflections of LSMO film and LAO substrate (obtained with $\text{CuK}\alpha$ radiation in laboratory diffractometer, at 0.5° incidence angle). The horizontal axis corresponds to 2θ angle, and vertical axis to ϕ angle. These axes are approximately following the [100]/[010] directions for 200 reflection, and [110]/[-110] for 110. The angular range for both 2θ and ϕ scans was 4° .

Figure 4. (a) Distribution histograms of the separation between consecutive misfit dislocations measured from the SEM images of the films of different thicknesses; and (b) dependence of the linear dislocation density versus the reciprocal film thickness (as measured by SEM (black symbols) and XRD: as estimated from the LSMO cell parameter value (green symbols) and from the satellite peak position (red symbols), along with the standard deviation of the distribution by SEM (blue symbols).

Figure 5. (a) HK Reciprocal space maps of $H\ 0\ 1$ ($H=1, 2, \text{ and } 3$) reflections of the LSMO film with 7 nm thickness; and (b) linear H scans of the different reflections $H\ 0\ 1$, from $H=1$ to 5, the scans are shifted to coincide in the H position of the LAO substrate at $H=1$ (the inset shows the same scans reduced dividing by H_0 ; along with (c) the corresponding model showing the overlap in the reciprocal space of fully strained and partially relaxed LSMO structures.

Figure 6. HK reciprocal space maps of the 101 and 111 reflections for the LSMO films with thickness 2.1 nm (a,d), 3.5 nm (b,e) and 7.0 nm (c,f). Maps were positioned at $L=0.95$ corresponding to the maximum of the LSMO contribution. (HKL in LAO reciprocal lattice units).

Figure 7. (a) In-plane diffraction 2θ - χ scans of the 200 reflection of the 7nm thick LSMO/LAO film using different incidence ω angles from 0.1 to 0.5°. (b) Integrated intensity ratio of the satellite component versus the 200 LSMO Bragg reflection. (c) Model of the depth distribution of the outer relaxed LSMO and buried strained-modulated LSMO structure.

Figure 8. Resistivity versus temperature measured in thin LSMO/LAO films with different thickness at 0T (black) and 9T (red) applied magnetic field. The arrows indicate for the 7 nm thick film the maximum of magnetoresistance corresponding to the coexistence of low and high T_c phases.

ASSOCIATED CONTENT

Supporting Information.

3D representation of reciprocal space maps of 002 symmetric and 113 asymmetric reflections for different film thickness measured at KMC-2 beamline at HZB (Bessy II).

This material is available free of charge via the Internet at <http://pubs.acs.org>.”

AUTHOR INFORMATION

Corresponding Author

* Corresponding author: José Santiso; ICN2, CSIC and BIST, Campus UAB 08193 Bellaterra, Barcelona, Spain. Phone: +34 93 7373634 <jose.santiso@icn2.cat>

Author Contributions

The manuscript was written through contributions of all authors. All authors have given approval to the final version of the manuscript.

ACKNOWLEDGMENT

This research was funded by the Spanish MINECO (projects: MAT2011-29081-C02, MAT2012-33207 and MAT2013-47869-C4-1-P, Consolider-Ingenio CSD2008-00023) and the European Union Horizon 2020 research and innovation programme under the Marie Skłodowska-Curie grant agreement No. 645658. We also acknowledge financial aid from the Generalitat de Catalunya (2014 SGR 501 and 2014 SGR 1216). J. S. thanks the support of Ministry of Education and Science through program “Salvador de Madariaga” for a grant (ref: PRX14/00297) to perform a stay at MIT. Z.K. is grateful for the support from the Ministry of Education, Science, and Technological Development of the Republic of Serbia through Project III45018. Q.L. and B.Y. thank the National Science Foundation for support through the MIT Center of Materials Science and Engineering MRSEC under grant no. DMR-1419807. This work made use of the Shared Experimental Facilities supported in part by the MRSEC Program of the National Science Foundation under award number DMR – 1419807. We thank Dr. Belén Ballesteros (ICN2, Barcelona) and Prof. Marie-Jo Casanova (CEMES, Toulouse) for their

assistance with transmission electron microscopy experiments. We are grateful to J. Rubio-Zuazo and the ESRF for providing assistance in using beamline BM25. We also thank HZB for the allocation of synchrotron radiation beamtime at Bessy.

REFERENCES

- (1) Schlom, D. G.; Chen, L. Q.; Eom, C. B.; Rabe, K. M.; Streiffer, S. K.; Triscone, J. M.. Strain Tuning of Ferroelectric Thin Films. *Annu. Rev. Mater. Res.*, **2007**, *37*, 589-626.
- (2) Jang, H. W.; Baek, S. H.; Ortiz, D.; Folkman, C. M.; Das, R. R.; Chu, Y. H.; Shafer, P.; Zhang, J. X.; Choudhury, S.; Vaithyanathan, V.; Chen, Y. B.; Felker, D. A.; Biegalski, M. D.; Rzchowski, M. S.; Pan, X. Q.; Schlom, D. G.; Chen, L. Q.; Ramesh, R.; Eom, C. B. Strain-Induced Polarization Rotation in Epitaxial (001) BiFeO₃ Thin Films. *Phys. Rev. Lett.*, **2008**, *10110*, 107602.
- (3) Bozovic, I.; Logvenov, G.; Belca, I.; Narimbetov, B.; Sveklo, I. Epitaxial Strain and Superconductivity in La_{2-x}Sr_xCuO₄ Thin Films. *Phys. Rev. Lett.*, **2002**, *89*, 107001.
- (4) Schlom, D. G.; Chen, L. Q.; Pan, X.; Schmehl, A.; Zurbuchen, M. A. (2008). A Thin Film Approach to Engineering Functionality into Oxides. *J. Amer. Ceram. Soc.* **2008**, *91*, 2429-2454.
- (5) Catalan, G.; Seidel, J.; Ramesh, R.; Scott, J. F. (2012). Domain Wall Nanoelectronics. *Rev. Mod. Phys.* **2012**, *84*, 119.
- (6) Farokhipoor, S.; Magén, C.; Venkatesan, S.; Íñiguez, J.; Daumont, C. J.; Rubi, D.; Snoeck, E.; Mostovoy, M.; de Graaf, C.; Müller, A.; Döblinger, M.; Scheu, C.; Noheda, B. Artificial Chemical and Magnetic Structure at the Domain Walls of an Epitaxial Oxide, *Nature* **2014**, *515*, 379–383.

(7) Arredondo, M.; Ramasse, Q. M.; Weyland, M.; Mahjoub, R.; Vrejoiu, I.; Hesse, D.; Browning, N. D.; Alexe, M.; Munroe, P.; Nagarajan, V. Direct Evidence for Cation Non-Stoichiometry and Cottrell Atmospheres Around Dislocation Cores in Functional Oxide Interfaces, *Adv. Mater.* **2010**, *22*, 2430–2434

(8) Chu, M. W.; Szafraniak, I.; Scholz, R.; Harnagea, C.; Hesse, D.; Alexe, M.; & Gösele, U.; Impact of Misfit Dislocations on the Polarization Instability of Epitaxial Nanostructured Ferroelectric Perovskites. *Nature Mater.*, **2004**, *3*, 87-90.

(9) Nagarajan, V.; Jia, C. L.; Kohlstedt, H.; Waser, R.; Misirlioglu, I. B.; Alpay, S. P.; Ramesh, R. Misfit Dislocations in Nanoscale Ferroelectric Heterostructures. *Appl. Phys. Lett.* **2005**, *86*, 192910

(10) Lubk, A.; Rossell, M. D.; Seidel, J.; Chu, Y. H.; Ramesh, R.; Hÿtch, M. J.; Snoeck, E. Electromechanical Coupling among Edge Dislocations, Domain Walls, and Nanodomains in BiFeO₃ Revealed by Unit-Cell-Wise Strain and Polarization Maps. *Nano Lett.* **2013**, *13*, 1410-1415.

(11) Chang, C. P.; Chu, M. W.; Jeng, H. T.; Cheng, S. L.; Lin, J. G.; Yang, J. R.; Chen, C. H. (2014). Condensation of Two-Dimensional Oxide-Interfacial Charges into One-Dimensional Electron Chains by the Misfit-Dislocation Strain Field. *Nature Comm.*, **2014**, *5*, 3522.

(12) Frank, F. C.; Van der Merwe, J. H. One-Dimensional Dislocations. II. Misfitting Monolayers and Oriented Overgrowth. In *Proc. Royal Soc. London A: Math., Phys. Eng. Sci.* **1949**, *198*, 216-225.

(13) Matthews, J. W.; Blakeslee, A. E. Defects in epitaxial multilayers: II. Dislocation Pile-ups, Threading Dislocations, Slip Lines and Cracks. *J. Crystal Growth*, **1975**, *29*, 273-280.

(14) Speck, J. S.; Pompe, W. Domain Configurations Due to Multiple Misfit Relaxation Mechanisms in Epitaxial Ferroelectric Thin Films. I. Theory. *J. Appl. Phys.* **1994**, *76*, 466-476.

- (15) Nabarro, F. R. N. Dislocations in a Simple Cubic Lattice. *Proc. Phys. Soc.*, **1947**, *59*, 256.
- (16) Kishinû, S.; Ogirima, M.; Kurata, K. A Cross-Hatch Pattern in GaAs_{1-x}P_x Epitaxially Grown on GaAs Substrate. *J. Electrochem. Soc.*; **1972**, *119*, 617-622.
- (17) Sánchez, F.; Garcia-Cuenca, M. V.; Ferrater, C.; Varela, M.; Herranz, G.; Martinez, B.; Fontcuberta, J. Transition from Three-to Two-Dimensional Growth in Strained SrRuO₃ Films on SrTiO₃ (001). *Appl. Phys. Lett.* **2003**, *83*, 902.
- (18) Kim, S. G.; Wang, Y.; and Chen, I.-W.; Strain Relaxation in Buried SrRuO₃ Layer in (Ca_{1-x}Sr_x)(Zr_{1-x}Ru_x)O₃/SrRuO₃/SrTiO₃ *Appl. Phys. Lett.* **2006**, *89*, 031905
- (19) Wang, Z. H.; Lebedev, O. I.; Van Tendeloo, G.; Cristiani, G.; Habermeier, H. U. Crosshatching on La_{0.5}Ca_{0.5}MnO₃ Ultrathin Films Epitaxially Grown on SrTiO₃(100). *Phys. Rev. B*, **2008**, *77*, 115330.
- (20) Sun, H. P.; Tian, W.; Pan, X. Q.; Haeni, J. H.; Schlom, D. G. Evolution of Dislocation Arrays in Epitaxial BaTiO₃ Thin Films Grown on (100)SrTiO₃. *Appl. Phys. Lett.* **2004**, *84*, 3298-3300
- (21) Tersoff, J.; Teichert, C.; Lagally, M. G. Self-Organization in Growth of Quantum Dot Superlattices. *Phys. Rev. Lett.* **1996**, *76*, 1675
- (22) Brune, H.; Giovannini, M.; Bromann, K.; Kern, K. Self-Organized Growth of Nanostructure Arrays on Strain-Relief Patterns. *Nature*, **1998**, *394*, 451-453.
- (23) Zhang, X, Liu, Z.; Li, Q.; Leung, Y.; Ip, K.; Hark, S. Routes to Grow Well-Aligned Arrays of ZnSe Nanowires and Nanorods. *Adv. Mater.*; **2005**, *17*, 1405-1410.
- (24) Meng, F.; Morin, S. A.; Forticaux, A.; Jin, S. Screw Dislocation Driven Growth of Nanomaterials. *Acc. Chem. Res.*; **2013**, *46*, 1616–1626

(25) Sandiumenge, F.; Santiso, J.; Balcells, L.; Konstantinovic, Z.; Roqueta, J.; Pomar, A.; Espinós, J. P.; Martínez, B. Competing Misfit Relaxation Mechanisms in Epitaxial Correlated Oxides. *Phys. Rev. Lett.* **2013**, *110*, 107206.

(26) Santiso, J.; Balcells, L.; Konstantinovic, Z.; Roqueta, J.; Ferrer, P.; Pomar, A.; Martínez, B.; Sandiumenge, F. Thickness Evolution of the Twin Structure and Shear Strain in LSMO films. *CrystEngComm*, **2013**, *15*, 3908-3918.

(27) Sandiumenge, F.; Bagués, N.; Santiso, J.; Paradinas, M.; Pomar, A.; Konstantinovic, Z.; Ocal, C.; Balcells, L.; Casanove, M.-J.; Martínez, B. Misfit Dislocation Guided Topographic and Conduction Patterning in Complex Oxide Epitaxial Thin Films" submitted to *Adv. Mater. Interfaces*. **2016**, 1600106; <http://dx.doi.org/10.1002/admi.201600106> (available online)

(28) MacPherson, G.; Goodhew, P. J.; Beanland, R. A Model for the Distribution of Misfit Dislocations Near Epitaxial Layer Interfaces. *Phil. Mag. A* **1995**, *72*, 1531-1545

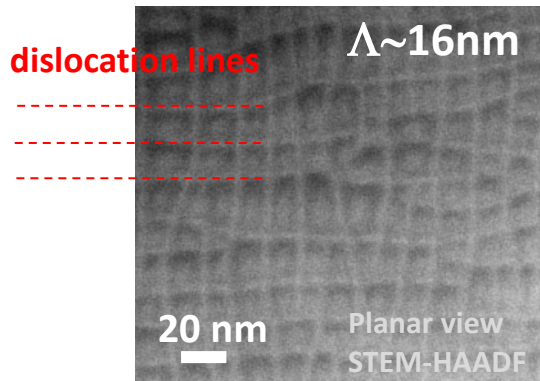
(29) Matthews, J. W.; Blakeslee, A. E. Defects in Epitaxial Multilayers: I. Misfit Dislocations. *J. Crystal Growth*, **1974**, *27*, 118-125.

(30) Ohring, M. Materials Science of Thin Films 2nd edn (New York: Academic). **2002**.

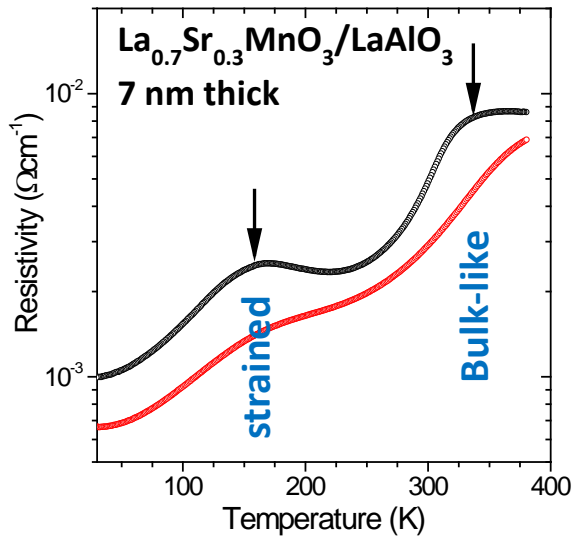
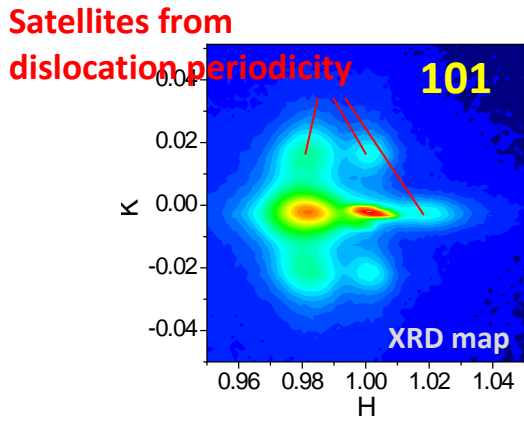
(31) Freund, L. B.; Dislocation Mechanisms of Relaxation in Strained Epitaxial Films, *MRS Bull.* **1992**, *17*, 52-60

(32) Fang, Z.; Solovyev, I. V.; Terakura, K. Phase Diagram of Tetragonal Manganites. *Phys. Rev. Lett.* **2000**, *84*, 3169

(33) Dong, L.; Schnitker, J.; Smith, R. W.; Srolovitz, D. J. Stress Relaxation and Misfit Dislocation Nucleation in the Growth of Misfitting Films: A Molecular Dynamics Simulation Study. *J. Appl. Phys.* **1998**, *83*, 217



Highly ordered array of misfit dislocations produces a nanophase composite with distinct functional properties than bulk



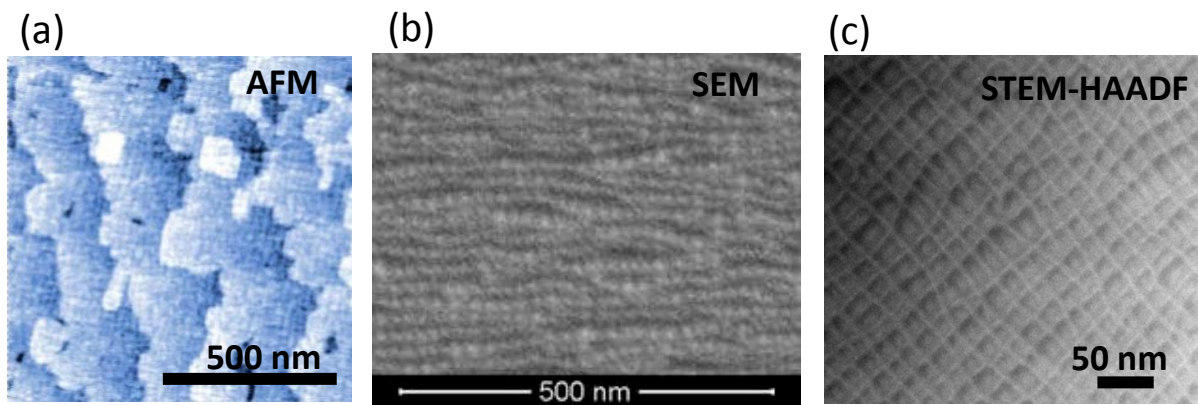


Figure 1. Planar view images of a 7 nm thick LSMO/LAO thin film with a well-developed misfit dislocation pattern as observed by AFM topography (a), orientation contrast SEM (b) and STEM taken at HAADF mode (c). In all cases the image contrast defines parallel lines that correspond to the position of the misfit dislocation cores parallel to $[100]$ and $[010]$ directions.

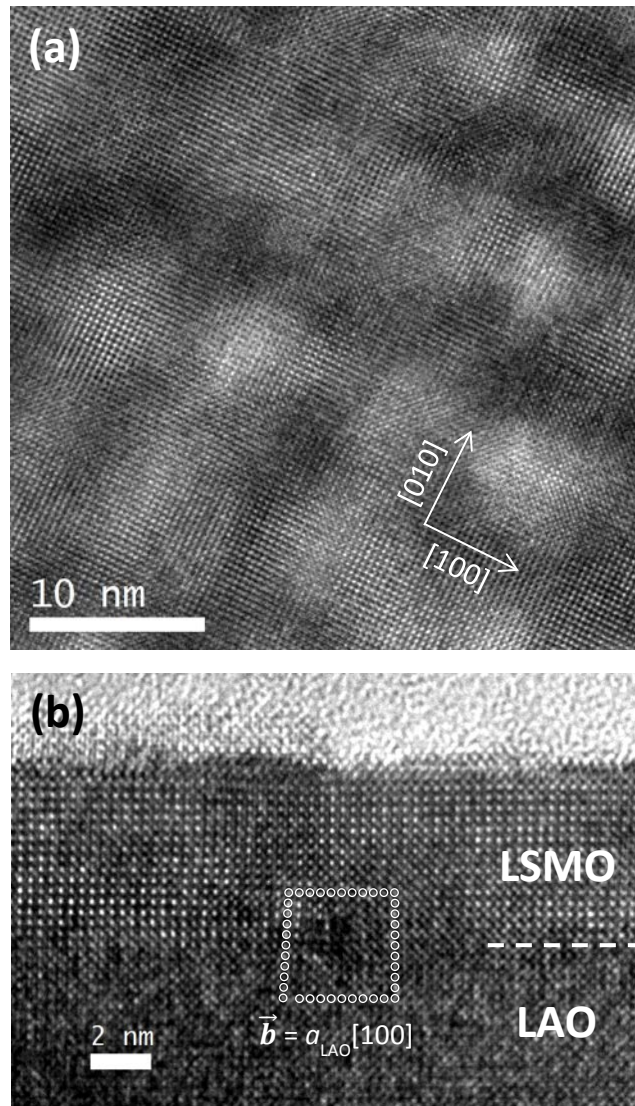


Figure 2. High-Resolution TEM images of a planar view (a) and cross-section (b) of a 7nm thick LSMO/LAO film. The cross-section shows a Burgers circuit around a misfit dislocation core at the film-substrate interface with a Burgers vector $\mathbf{b} = a_{\text{LAO}}[100]$.

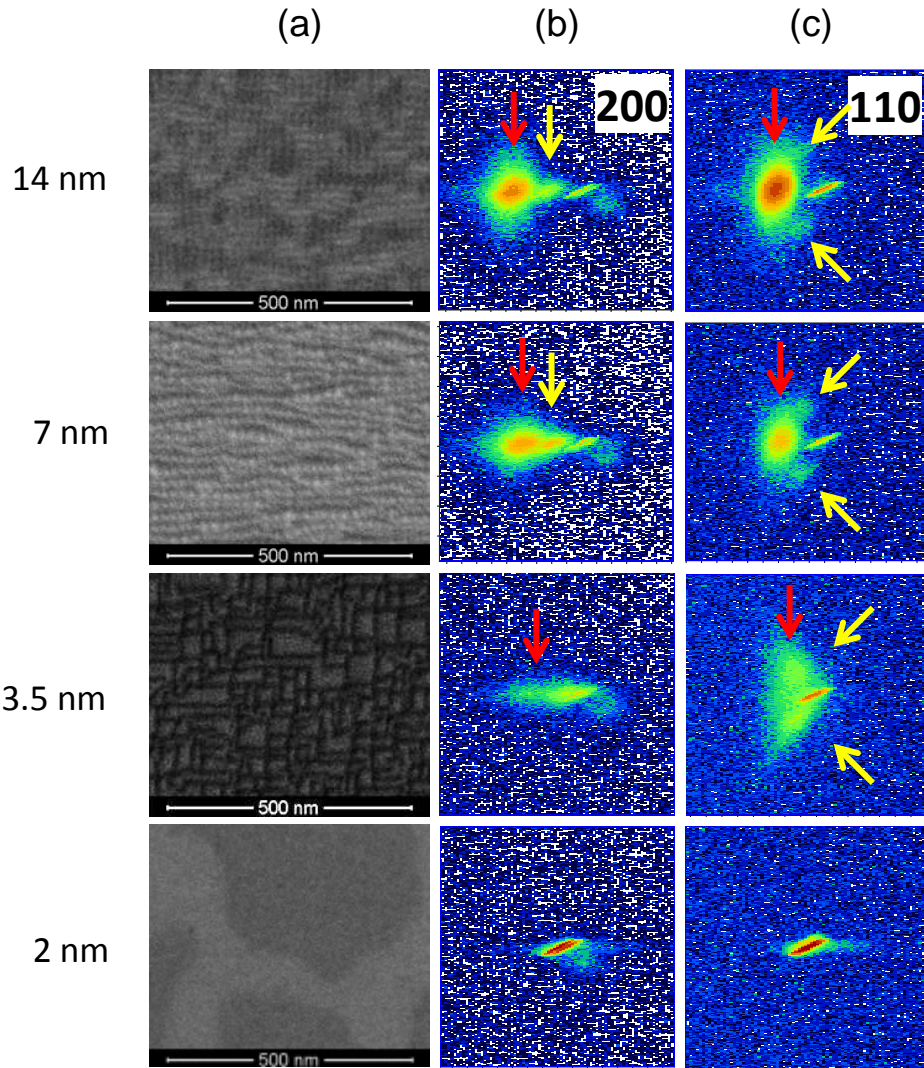


Figure 3. The chart shows details of LSMO films with different thicknesses from 2, 3.5, 7 and 14 nm. In columns (from left to right): (a) Orientation contrast-SEM images of the same samples. The observed horizontal and vertical lines correspond to misfit dislocations running parallel to [100] and [010] crystallographic directions; In-plane XRD 2θ - ϕ area of 200 (b) and 110 (c) reflections of LSMO film and LAO substrate (obtained with $\text{CuK}\alpha$ radiation in laboratory diffractometer, at 0.5° incidence angle). The horizontal axis corresponds to 2θ angle, and vertical axis to ϕ angle. These axes are approximately following the [100]/[010] directions for 200 reflection, and [110]/[-110] for 110. The angular range for both 2θ and ϕ scans was 4° .

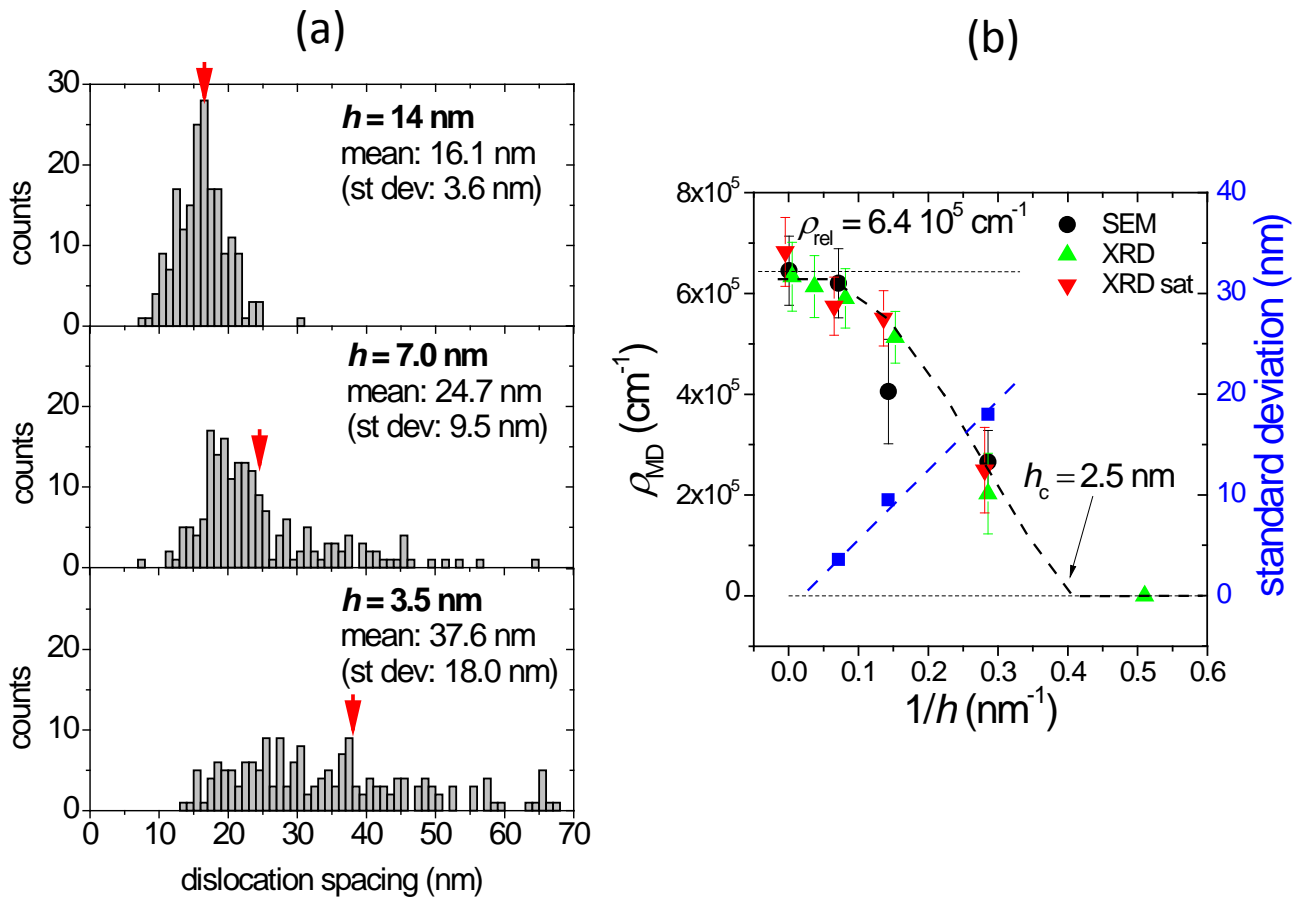


Figure 4. (a) Distribution histograms of the separation between consecutive misfit dislocations measured from the SEM images of the films of different thicknesses; and (b) dependence of the linear dislocation density versus the reciprocal film thickness (as measured by SEM (black symbols) and XRD: as estimated from the LSMO cell parameter value (green symbols) and from the satellite peak position (red symbols), along with the standard deviation of the distribution by SEM (blue symbols).

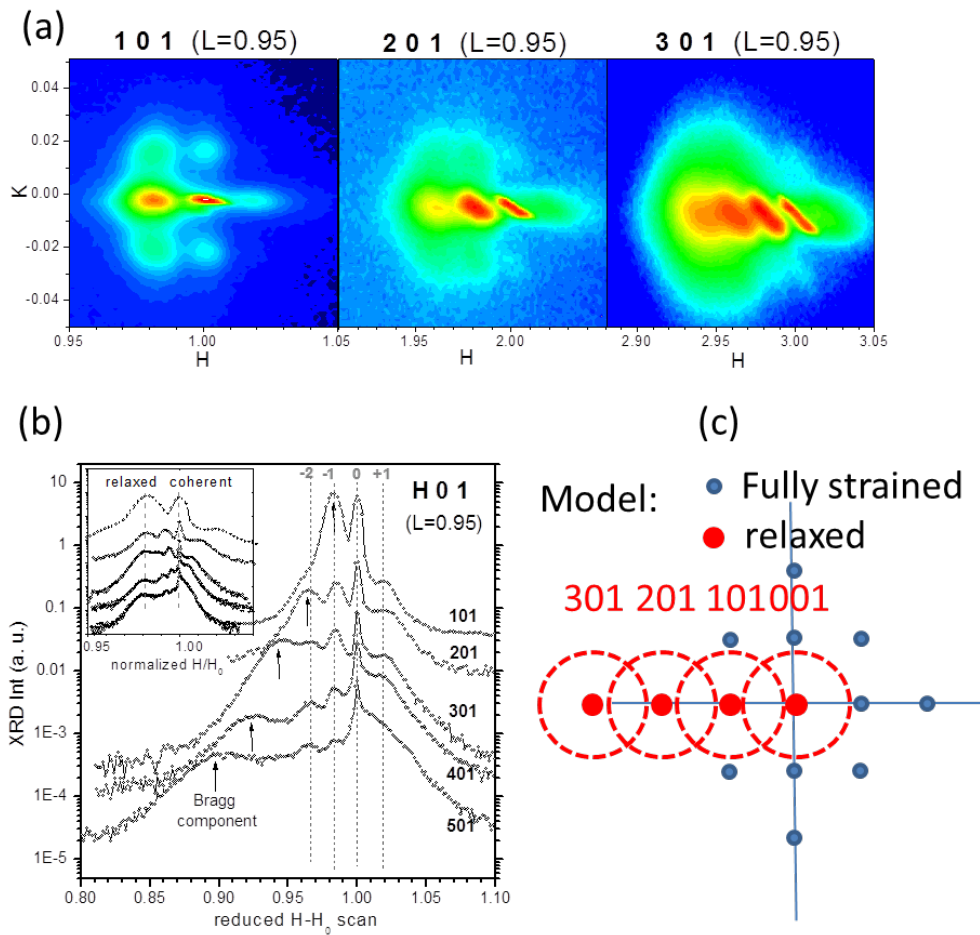


Figure 5. (a) HK Reciprocal space maps of $H01$ ($H=1, 2,$ and 3) reflections of the LSMO film with 7 nm thickness; and (b) linear H scans of the different reflections $H01$, from $H=1$ to 5 , the scans are shifted to coincide in the H position of the LAO substrate at $H=1$ (the inset shows the same scans reduced dividing by H_0); along with (c) the corresponding model showing the overlap in the reciprocal space of fully strained and partially relaxed LSMO structures.

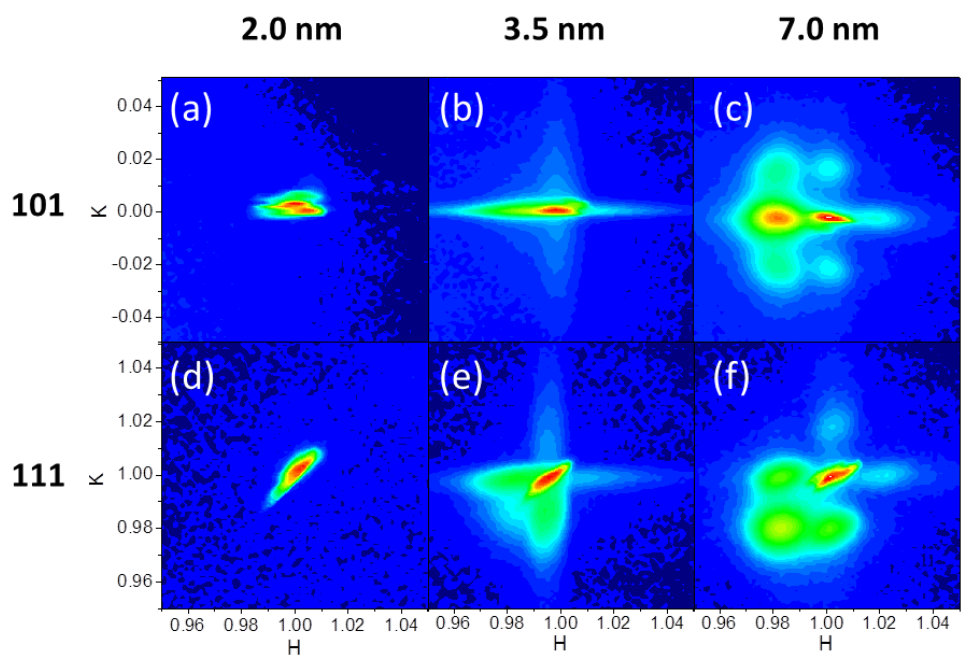


Figure 6. HK reciprocal space maps of the 101 and 111 reflections for the LSMO films with thickness 2.1 nm (a,d), 3.5 nm (b,e) and 7.0 nm (c,f). Maps were positioned at $L=0.95$ corresponding to the maximum of the LSMO contribution. (HKL in LAO reciprocal lattice units)

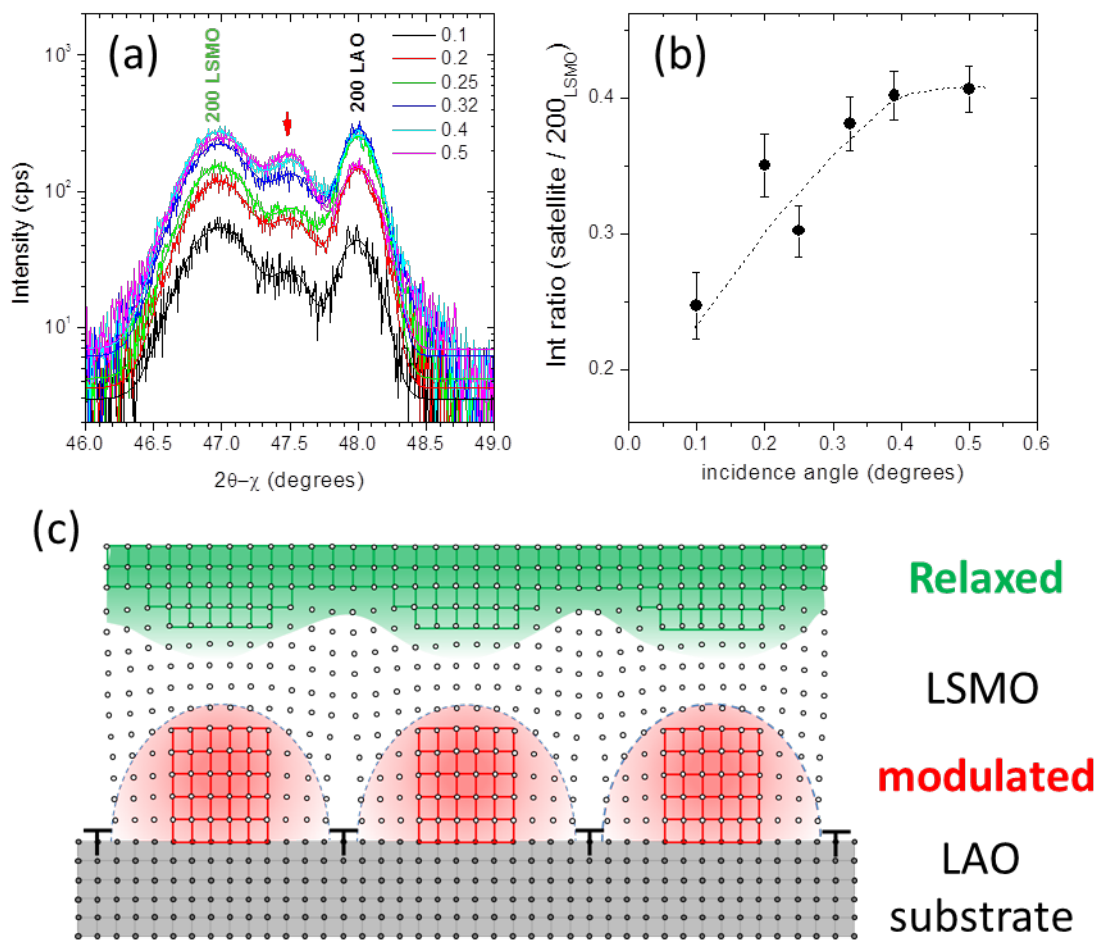


Figure 7. (a) In-plane diffraction $2\theta-\chi$ scans of the 200 reflection of the 7nm thick LSMO/LAO film using different incidence ω angles from 0.1 to 0.5°. (b) Integrated intensity ratio of the satellite component versus the 200 LSMO Bragg reflection. (c) Model of the depth distribution of the outer relaxed LSMO and buried strained-modulated LSMO structure.

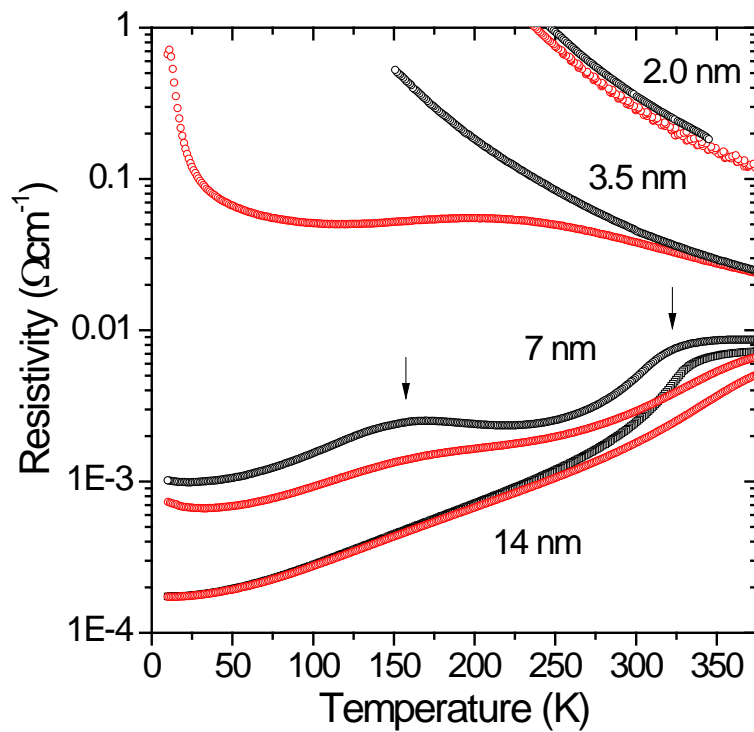


Figure 8. Resistivity versus temperature measured in thin LSMO/LAO films with different thickness at 0T (black) and 9T (red) applied magnetic field. The arrows indicate for the 7 nm thick film the maximum of magnetoresistance corresponding to the coexistence of low and high T_c phases.